WWW.PVAMU.EDU/PURSUE

Volume 1 Issue 1 2017

PURSUE

UNDERGRADUATE RESEARCH JOURNAL

PURSUE

Undergraduate Research Journal

AIM AND SCOPE

The scholarly journal, "PURSUE", provides undergraduates an avenue to publish their original research articles in the following areas: (but not limited to) psychology, sociology, biology, chemistry, physics, engineering, computer science, mathematics, humanities, agriculture, architecture, business, and education.

The original research articles included in this journal are peer-reviewed and selected by the journal's Editorial Board. The review process allows undergraduate researchers to receive feedback from notable scientists in their field of study and teach them about the publication process. Publishing their work will not only inform the scientific community but also impact the greater society.

The journal is housed at Prairie View A&M University, a Historically Black University, and is available to all young scientists conducting research. This journal also serves as a means for faculty to extend knowledge beyond the classroom and encourage other students to conduct quality research. All undergraduate research is produced in conjunction with a faculty mentor and is peer reviewed. The journal is open to undergraduates from all Colleges and Universities.

PURSUE

Undergraduate Research Journal
Volume 1, Issue 1, 2017

CONTENTS

FROM THE

EXECUTIVE EDITOR

Dear Readers,

I am pleased to share with you the scholarly journal PURSUE, which provides student research scientists with an avenue to publish their original research articles. From psychology, sociology, and humanities to agriculture, biology, chemistry, engineering and beyond, this journal is designed to inform the community and impact the greater society.

I congratulate our undergraduate writers who contributed to this edition of PURSUE, and I express my sincere gratitude to the faculty mentors who supported these students in their research journeys. As educators, it is our duty to give students opportunities to showcase their knowledge, and this journal does just that, by extending their comprehension beyond the classroom and out into the world.

It is my wish that through PURSUE, each reader will be inspired to undertake a lifelong journey of exploration and discovery. Enjoy it to the fullest.

Felecia M. Nave
Executive Editor, PURSUE
Provost & Senior Vice President for Academic Affairs
Prairie View A&M University

FROM THE

MANAGING EDITORS

PURSUE has launched!

We are honored to have worked with a wonderful Editorial Board and an expert team of Review Editors to produce this exciting new undergraduate research journal, PURSUE!

As a result of several years of experience working with undergraduate students, we know first-hand how difficult it can be for them to publish research when having to compete with graduate students and professional scientists. PURSUE aims to change that! As an undergraduate research journal, students will be the first authors for all of our publications. It is our hope that PURSUE will inspire all undergraduate students to conduct research and submit manuscripts for publication. We also hope it inspires faculty to work more with undergraduates.

We celebrate each undergraduate author in this inaugural issue as a "Pioneer" and thank him or her for serving as an excellent example of undergraduate scholarship.

Respectfully,
Audie Thompson, Ph.D.
Yolander Youngblood, Ph.D.

PURSUE

Undergraduate Research Journal

This journal is published with the generous support of the Office for Academic Affairs at Prairie View A&M University

Square or not Square--That's the Question!

Alexandra Cromer,[1] Falonne Moumbogno T. Colbie,[1] Nia Parker,[1] Steven Wang,[2] Hao Wu,[3] Hua-Jun Fan[1]

[1]Prairie View A&M University, [2]Cypress Ranch High School 2016 Summer Internship, [3]Ningbo University of Technology

Corresponding Author: Hua-Jun Fan, Department of Chemistry, Prairie View A&M University, PO Box 519; MS 2215, Prairie View, TX 77446; Phone: (936) 261-3111; Email: hjfan@pvamu.edu

Abstract

Background: Most heavy metals from industrial catalysts are harmful to human body; however, to function normally, the human body *does* need traces of essential metal cofactors. Histidine is one of the nine essential amino acids to the human body, and cobalt(II) ion is cost effective and is known to be less toxic to the body. **Methods:** This project investigates the binding reactions between the cobalt(II) ion and histidine amino acids. Due to unsuccessful attempts to crystalize Cobalt(II)-Histidine complex in the lab, the quantum mechanics modeling package, G09, was employed to provide the binding mode and interaction between the metal and histidine complex. Geometric parameters were attained in order to predict the crystal structure the complex. **Results:** The data confirms that complexes between cobalt ions and deprotonated histidine will only settle into a square planar geometry, regardless of the initial geometry. However, with neutral histidine, the complex is not in square planar formation at all. Instead, the five-member ring formed among cobalt and histidine's N- and C-terminus forms an angle, where N-Co-N is almost linear (167.5°). **Conclusion:** Different reaction conditions will yield either tetrahedral and square planar geometry at the metal center, which will influence the band gap. Such influence can then be used to create a tunable and broad-spectrum solar panel materials.

Keywords: Density functional theory, cobalt(II), histidine, binding mode, electronic structure

Introduction

Proteins are very important for the wellness of humans and are the building blocks of amino acids. In fact, 20% of the human body is made of proteins, and they play crucial role in the biological processes.[1] In fact, a large proportion of protein in the human body comprises muscles, cells and tissues, all with their unique amino acid structures. Protein functions include giving cells structure, wound healing, transport and storage of nutrients and much more.[2] Histidine is one of the nine essential amino acids that cannot be synthesized in the human body; thus, it must be consumed. One of the critical needs of histidine is its role in the formation of hemoglobin and its assist with the formation and repair of tissues.

Certain trace metals are essential elements of well-being for human body, while some heavy metals are harmful to human body. Maximum Contaminant Levels (MCL) standards for the most hazardous heavy metals are set by the United States Environmental Protection Agency (EPA).[3] Toxicity refers to the amount of the metal the body can take before being poisoned. This legal threshold toxicity limits are usually expressed as a concentration in milligrams per liter of water. The larger the concentration, the more of the metal it takes to poison the body. The transition metal cobalt is toxic at levels higher than 1.0 MCL (mg/L), and it is known to be related to cardiomyopathy, deafness, nerve conditions, tinnitus, blood thickening, and thyroid dysfunctions when found at toxic levels in the human body. Cobalt, a relatively cheap heavy metal, can bind to the amino acid histidine.[4] Because the MCL for cobalt is so high, this reflects the low toxicity of cobalt compared to other heavy metals such as mercury, lead, or arsenic.

In this study, the binding mode between the cobalt (II) ion with histidine will be investigated through a computational modeling approach. The binding geometry and electronic structure of this binding complex will provide the insights on how the amino acid binds to the metal centers and the strength of the binding. This work has implications for both environmental and cellular biology.

Materials and Methods

All molecules and transition states are constructed using GaussView (Gaussian, Inc., Wallingford CT) optimized with the Gaussian 09 package.[5] The popular B3LYP[6] with hybrid exchange functional were used for all geometry optimization and frequency calculations. B3LYP is a hybrid functional that was developed in the late 1980s in order to eliminate the downsides that the other hybrid correlation functionals face when calculating electron correlation. B3LYP is used in computational molecular work, where it is used widely because of its relative versatility and speed, even when compared to more recent hybrid functionals.

All structures were fully optimized and frequency analyses were performed to ensure either a *minimum* was achieved, which had zero imaginary vibrational frequency as derived from a vibrational frequency analysis, or *transition state* was identified, which had one imaginary vibrational frequency.

The vibrational mode was visualized to confirm the expected motion of transition state. A separate intrinsic reaction coordinate (IRC) calculation was then performed on the transition state geometry to follow either the forward or reverse vibrational mode into the local minimum. The thermodynamic parameters of the reaction, such as zero point corrected energy ([ΔE^{ZPE}], enthalpies [$\Delta H°$], and Gibbs Free energies [$\Delta G°$]), were calculated at 298.15 K and 1 atm.

A basis set is a set of functions that are used to calculate molecular orbitals accurately. The basis sets used were 6-31g* and LANL2DZ. The basis set 6-31g* was used for the C, N, H, and O while a split basis set LANL2DZ was used for the Ni(II) and core electrons uses LANL2DZ effective core potential.

Results

According to the Ligand Field Theory (LFT, also known as Crystal Field Theory), when ligands approach the central metal ion to form a complex, due to the electron-electron repulsion, the previous degenerate five d-orbitals will split according to the approaching

direction of ligand and orientation of the d-orbitals. This is also the foundation of group theory where the reducible and irreducible representation was generated and dissected. As shown in Figure 1, in ***octahedral*** geometry, when six ligands approach the central atom, the 5 d-orbitals of the central metal ion will split into two sets: one set consists of d_{z2} and d_{x2-y2} orbitals, while the other set consists of three orbital: d_{xy}, d_{yz}, and d_{xy}. In the ***tetrahedral*** geometry, where four ligands approach the metal ion, the split pattern flips, but it still maintains two sets of splitting orbitals. However, this splitting pattern gets much more complicated when the same four ligands approach the central metal ion to form a square planar geometry. In this formation, not only the d_{z2} and d_{x2-y2} set of orbitals further split, but now the d_{xy} orbital is higher in energy than d_{z2}. All of these splitting patterns are based on the amount of "imaginary" collision between the central metal ion and incoming ligand when the complex is formed. However, such "imaginary" collision shall not be confused with the coordination bond formed in the complex.

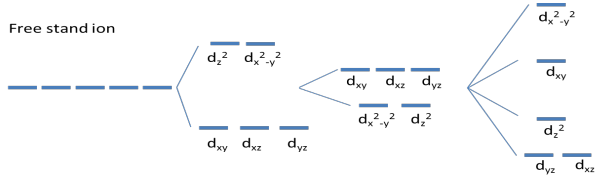

Figure 1 Five d-orbital splitting pattern in the different geometry according to the Ligand Field Theory

Splitting due to asymmetric electronic structure

One should also keep in mind that not only the geometric arrangement can distort (*aka* splitting) the electronic structure and d-electron arrangement; the unpaired electrons in the d-orbital would have the same electronic distortion on the free stand metal ion. For example, the cobalt (II) ion has seven (7) d-electrons. While the Hund's rule would like to keep the d-orbitals in degeneracy, the odd number of d-electrons would destroy the degeneracy and create a splitting pattern that depends on the electron repulsion and coupling.

The modeling results in Figure 2 demonstrates the d-orbital splitting pattern of free stand Co(II) are due to the asymmetric electronic structure. The left panel has Co(II) in doublet, where there is only one unpaired electron; meanwhile, the right panel is Co(II) in quadruplet, where there are three unpaired electrons. The modeling results show that doublet is 53.2 kcal/mol higher in Gibbs Free energy than that of quadruplet. This suggests that the free standing Co(II) would have high spin state.

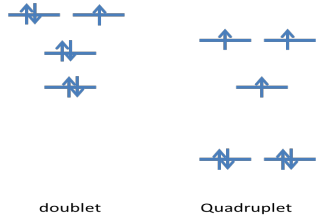

Figure 2 The d-orbital splitting pattern calculated for Co(II) due to asymmetric electronic structure

Deprotonation of histidine

Because the LFT explains the electronic structure of the complex, especially the d-orbital splitting pattern of the central metal ion, it provides an insight to the geometry around the metal center or electronic structure at the metal center. However, for any ligand to bond with metal, these ligands must have lone pairs of electrons. The histidine has a few locations that enable it to bind with metal—namely, the oxygen atoms on carboxylate portion of C-terminus, the nitrogen atom on amine group of N-terminus, and nitrogen atoms of R-group. As shown on the left in Figure 3, the neutral histidine optimized in the gas phase was not in Zwitterion (aka dipolar ion). When deprotonated (right in Figure 3) the Gibbs Free energy required is 350.6 kcal/mol. We believe the energy would be lowered when compensated by the Polarizable Continuum Model (PCM) using the integral equation formalism variant (IEFPCM) model using SCRF keyword where the charges will be solvated to further stabilize the ions.

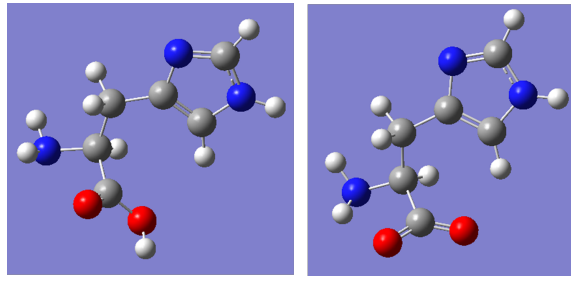

Figure 3 The optimized geometries of neutral histidine (left) and deprotonated (+1 charge) of histidine (right).

The optimized bond lengths of the neutral histidine and deprotonated histidine are listed in table 1. As one can imagine it, the only significant bond length changes would be around the carboxylate group where C1-O1 bond length significantly decreased from 1.3553 Å to 1.2588 Å upon deprotonation, while the other C1-O2 bond length slightly increased from 1.2108 Å to 1.2579 Å. The C1-C2 bond also increases from 1.5254 Å to 1.5846 Å. This suggests that upon the deprotonation, the electron lone pair used to bind the proton is re-distributed to the other C-O and C-C bonds of carboxylate group. The rest moiety of histidine does not change or shows less than hundredth Å changes.

Table 1 The geometry parameters of neutral histidine and deprotonated histidine

	Neutral Histidine	Deprotonated Histidine
O1-C1	1.35531	1.25882
C1-O2	1.21083	1.25789
C1-C2	1.52544	1.58464
C2-N1	1.46898	1.47419
C2-C3	1.545	1.55239
C3-C4	1.50336	1.50457
C4-N2	1.38424	1.3916
N2-C5	1.31349	1.31542
C5-N3	1.36479	1.36801
N3-C6	1.38185	1.38269
C6-C4	1.37611	1.37442

As mentioned earlier, there are three available binding sites on histidine: C-terminus, N-terminus, and nitrogen atoms on the R fragments. In this paper, the focus is on the C-terminus and N-terminus binding to the Co(II). For comparison, both the neutral histidine and deprotonated histidine binding to metal were investigated and presented here.

Binding Co(II) with neutral protonated histidine

When the neutral protonated histidine binds to the metal center, both form a 5-member ring that consists of the metal ion, N-terminus, α-carbon, and C-terminus forms as shown in Figure 4**a**. For the sake of clarity, a different view angle of same geometry is shown Figure 4**b,** where hydrogens are not shown. It is interesting to point out that two five-member rings are not in the same plane, instead they are angled. The N1-Co-N1' bond angle is 167.5°,O1-Co-O1' bond angle is 113.3°, and N1-Co-O1 bond angle is 76.0°. The overall geometry of this complex can be classified as boat configuration, because the Co-$^{\alpha}$C-H bond in the five-member ring is 94.1°, which is axial H on the α carbon. Relative to quadruplet state of Co(II), this binding mode has interaction energy of ΔG = -295.5 kcal/mol, which suggests a strong interaction.

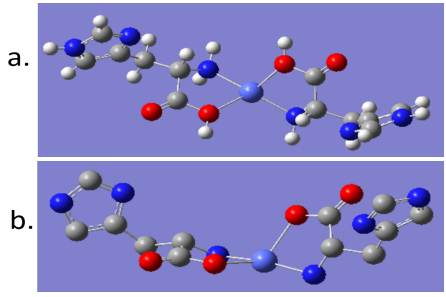

Figure 4 Optimized geometry of Cobalt (II)-neutral histidine complexes in (a). The hydrogen atoms are omitted for clarification in (b) as well as in a side-view angle

Binding Co(II) with deprotonated histidine

However, the geometry at the metal center of deprotonated histidine is drastically different than that geometry of neutral histidine complex as shown in Figure 4. As a matter of fact, the metal center of deprotonated histidine always shows a square planar geometry. Two 5-member ring that consists of the metal ion, N-terminus, α-carbon, and C-terminus of histidine are almost planar to each other. For example, the N1-Co-N1' bond angle is 179.0°, O1-Co-O1' bond angle is 178.2°, and N1-Co-O1 bond angle is 85.9° (Figure 5a). Interestingly, there are three different conformations identified for this deprotonated-Co complex as shown in Again, for the sake of clarification, all hydrogen atoms are not shown in the figure. The optimized bond lengths of these three conformations are shown in Table 2. One can see that the bond lengths of Co-N1 and Co-O1 are both longer in conformation b and c than those in conformation a. Even more interesting, the Co-N1 bond length is longer in conformation c than that in conformation b. This suggests that there is trans effect of carboxylate group that weakens the Co-N1 bond. This is evidenced that Co-O1 bond length almost identical between conformations b and c while the Co-N1 bond length is longer in conformation c (2.00506 Å) than that of b (1.97665 Å).

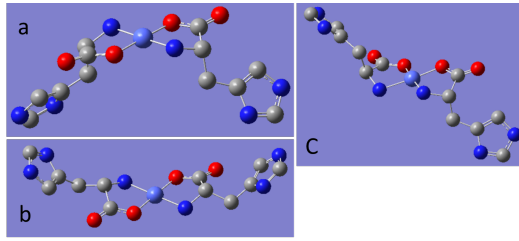

Figure 5 Three different binding modes of deprotonated histidine with cobalt (II) ion

As shown in Figure 5, the two histidine amino acids take *trans* form to each other in both conformations *a* and *b*. For example, the N-terminus of one histidine is trans to the N-terminus of the other histidine. However, the calculated conformation *c* has a *cis* form, where the N-terminus of one histidine is *cis* to the N-terminus of the other histidine. As a result, the conformation *c* is drastically different from those of conformations *a* and *b*. Furthermore, even the conformations *a* and *b* are slight different in their final geometry, as the R-group is slight bent up in conformation *b*. Carefully examining the optimized conformations *a* and *b* reveals that the M-$^{\alpha}$C-H bond angle may be a determining factor. For example, the M-$^{\alpha}$C-H bond angle of conformation *a* is 142°. This can be seen as an equatorial position. On the other hand, the M-$^{\alpha}$C-H bond angle of conformation *b* is 97°, which is an axial position. The M-$^{\alpha}$C-H bond angle of conformation *c* is a mixture of axial and equatorial position, which is 137 and 98 degrees.

Table 2 The optimized bond lengths of three different conformations of deprotonated Histidine complex

Conformation	a	b	c
O1-C1	1.31707	1.30885	1.30371
C1-O2	1.21919	1.22172	1.22279
C1-C2	1.55033	1.55322	1.55085
C2-N1	1.49724	1.49849	1.50395
C2-C3	1.5433	1.54092	1.54089
C3-C4	1.50435	1.50326	1.50387
C4-N2	1.38347	1.38376	1.38312
N2-C5	1.31454	1.31528	1.31504
C5-N3	1.36561	1.36637	1.36567
N3-C6	1.37945	1.37877	1.3787
C6-C4	1.37593	1.37567	1.37601
N1-Metal	1.96087	1.97665	2.00506
O1-Metal	1.85192	1.87456	1.87467
O1'-C1'	1.31708	1.30884	1.3037
C1'-O2'	1.21919	1.22172	1.2228
C1'-C2'	1.55033	1.55319	1.55084
C2'-N1'	1.49722	1.49846	1.50395
C2'-C3'	1.54331	1.54092	1.5409
C3'-C4'	1.50434	1.50326	1.50387
C4'-N2'	1.38346	1.38376	1.38312
N2'-C5'	1.31455	1.31528	1.31504
C5'-N3'	1.36561	1.36637	1.36567
N3'-C6'	1.37945	1.37877	1.3787
C6'-C4'	1.37593	1.37567	1.37601
N1'-Metal	1.96085	1.97669	2.0051
O1'-Metal	1.85186	1.8746	1.87465

Conclusions

In this study, the binding mode between the cobalt (II) ion with histidine was thoroughly investigated through computational modeling. The results demonstrated that complexes between cobalt ion and deprotonated histidine will only settle into a square planar geometry, regardless the initial geometry. However, with neutral histidine, the complex is not square planar at all. Instead, the five-member ring formed among cobalt and histidine's N- and C-terminus forms an angle, where N-Co-N is almost linear (167.5°).

These findings can assist in designing the wide spectrum solar energy materials with tunable energy gap. By modifying the reaction conditions, one can achieve a desirable geometry conformation between the histidine and metals. Such geometries such as the tetrahedral and square planar can yield specific band gap that convert the particular wavelength of sunlight into electricity.

Acknowledgements

We gratefully acknowledge the Department of Chemistry at Prairie View A&M University for release time and funding support of this work. Other financial support includes the 2014 and 2016 PVAMU Summer Research Mini-grant, the U.S. Department of Energy, National Nuclear Security Administration grant (DE-NA 0001861 & DE-NA 0002630), and the Welch Foundation Grant (#L0002).

References

1 Erdmann, R. & Jones, M. *The Amino Revolution*. First Fireside Edition edn, 2 (1987).

2 Jones, L. & Atkins, P. in *Chemistry: Molecules, Matter and Change* (WH Freeman, 2000).

3 Barakat, M. New trends in removing heavy metals from industrial wastewater. *Arabian Journal of Chemistry* **4**, 361-377, doi:doi:10.1016/j.arabjc.2010.07.019 (2010).

4 Registry, A. f. T. S. a. D. Toxicological profile for cobalt. (US Department of Health and Human Services/Public Health Service, Atlanta, GA, 2004).

5 Frisch, M. *et al*. *Gaussian 09*. (Gaussian, Inc, 2009).

6 Becke, A. A new mixing of Hartree-Fock and local density funtional theories. *Journal of Chemistry and Physics* **98**, 1372-1377, doi:doi: http://dx.doi.org/10.1063/1.464304 (1993).

Assessment of Keratitis Damage in an Age Dependent Mouse Model Using Analytical Software

Quincy C. Moore III, PhD,[1] Emmanuel B. Olorunyomi,[1] Miles E. DuBose,[2] and Cleveland O. Lane Jr, PhD[1]

[1]Prairie View A & M University
[2]2016 Research Experience for High School Students (REH) Program, Prairie View A&M University

Corresponding Author: Quincy C Moore III, Ph.D., Department of Biology, Prairie View A & M University, PO BOX 519: MS 2210, Prairie View, TX 77446; Phone: (936) 261-3168; Fax: (936) 261- 3179; Email: qcmoore@pvamu.edu

Abstract

Background: *Streptococcus pneumoniae* (pneumococcus) is a gram-positive bacterium that is responsible for diseases such as, otitis media, conjunctivitis, bacterial keratitis, pneumonia, and meningitis. Bacterial keratitis is one of the most common after-effects of trauma to the eye. Some reports have shown the *S. pneumoniae* spreads through enzymes that are produced to digest the cornea, which in turn can causes blindness. There is a need for more improved measures that can reverse the detrimental effects of the bacteria. The long-term goal of this research is to better understand the complete role of *S. pneumoniae* and its components in bacterial keratitis to develop next generation therapies to prevent blindness. The purpose of this study is to develop alternative measures to evaluate damage associated with keratitis infection by use of computer applications. **Methods:** This study analyzed images of the established Keratitis pneumococcal mouse model. The eye images of mice 7-8-week-old and 9-month-old were collected. Additional images were taken on post-infection days one, three, five, and nine, revealing the progression of the infection. **Results:** The ImageJ Application provided more in depth review to determine the detrimental effects of *S. pneumoniae*. Through the software, a "Color Threshold" was created on every image to emphasize the area of damage caused by the bacteria. A scatter plot of every image created a map of the

particles, and the diameter created a scale demonstrating the impact of keratitis. Data revealed that the most significant increase in infection occurs between Day 1 and 3 post-infection. **Conclusions:** The study has created a computer model to establish a baseline for the infection process of *S. pneumoniae* in the traditional mouse model. ImageJ has proven to be a useful tool to analyze the impact of disease on the murine model. Results from this study also provide evidence of the importance of early intervention in ocular disease.

Keywords: ImageJ, *Streptococcus pneumoniae,* keratitis, aging

Introduction

Ocular infections such as keratitis, conjunctivitis, and endophthalmitis are caused by an opportunistic pathogen known as *Streptococcus pneumoniae*. *S. pneumoniae* is considered one of the leading bacterial causes of keratitis, which is a serious ocular infectious disease.[1,2] There is a poor clinical outcome of the patients suffering from bacterial keratitis that do not seek immediate medical care.[3] The incidence of ocular morbidity and blindness worldwide is related to infections of the cornea. Traditionally, pneumococcal infections affect elderly individuals or young children due to their weakened immune systems.[4] The elderly population is more susceptible to microbial keratitis than younger patients, because they are more likely to have had previous or co-existent ocular disease or surgery.[5] Consequently, visual outcome is significantly worse in older patients.[5] Aging is also strongly associated with alterations in the structure and function of the eye and with the development of ocular diseases.[6] Various *in vivo* models of aging have been described and developed in *Pseudomonas* and *Staphylococcus aureus* keratitis models. The studies demonstrated the inability of the immune cells to fight off infection and increased pathology in the aged mice.[7,8]

Wayne Rasband of the National Institute of Mental Health developed ImageJ (NIH, Bethesda, Maryland), which is a public domain Java-based image processing and analysis program.[9,10] ImageJ has been extensively used for image processing in immunohistochemistry,[10] tissue segmentation in microscopy

images,[11] and muscle morphometric measurements.[11] Use of this sophisticated software offers a refinement in the use of animal models in respect to determining the time-points for treatment of infection. The software offers the possibility for biomedical modeling of keratitis to predict outcome that will occur in the ocular environment.

The long-term goal of this research is to better understand the complete role of *S. pneumoniae* and its components in keratitis and to develop next generation therapies to prevent blindness. The purpose of this study is to develop alternative measures to evaluate damage associated with keratitis infection by computer application compared to the established keratitis pneumococcal mouse model. The study evaluates the progression of ocular damage with analytical software, ImageJ Application, which measures the diameter of the infection, from early to late progression of disease in both young and old murine models.

Materials and Methods

Sample Population and Analysis

Male and female C57BL/6 (Harlan, Houston, TX) were used in this study represented two age groups consisting of young mice (7-8-week-old) and old mice (9-month-old). The ocular images range from 1, 3, and 5 days post-infection. During experimentation, all animals were maintained according to institutional guidelines approved by the Institutional Animal Care and Use Committee (IACUC) approved protocol 2013-04010-101 (Prairie View A&M University) and the tenets of the Association for Research in Vision and Ophthalmology (ARVO) Resolution on the Use of Animals in Ophthalmic and Vision Research. Mouse eyes were infected using a protocol utilizing the established scratch mouse model.[12] The .jpeg images of the infected eyes from the aging study conducted were utilized for the analysis. The photos of the ocular images were visualized in ImageJ by cropping the photo to view the infection site. After the appropriate size was determined, an 8-bit photo filter was utilized to make the color black and white. Following the image color change, the image was adjusted using “Auto Threshold” and

the photo option that displays the proper black and white particles was chosen. The particles were analyzed with the "Analyze Particles" option. To continue the evaluation of the ocular image, the "Scatter Plot" option was utilized, and the tool for "Outlines" generates the data plotted as numbers. The diameter of the infection site was measured using the straight-line tool to draw a line. The infection site was visualized from a majority of particles that is surrounding the cornea to make a circle and using the "Analyze" tool the diameter was measured. The data collected was transferred to excel spreadsheet for analysis (figure 1).

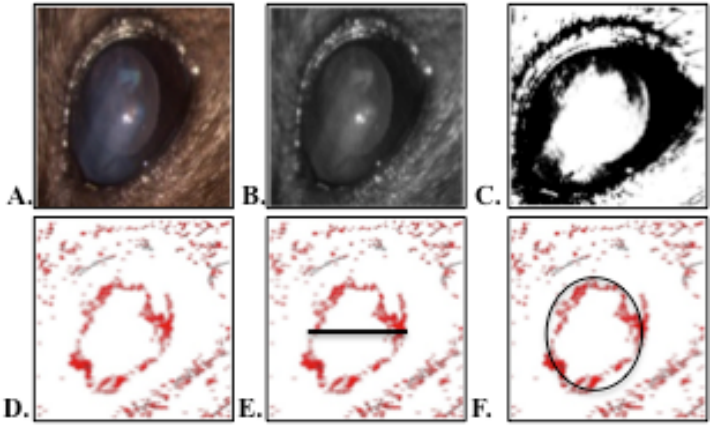

Figure 1 Sample Analysis. **A.** Selected ocular image for analysis. **B.** Image was converted to black and white using an 8-bit photo filter. **C.** Image adjusted using the "Auto Threshold" option displaying the black and white particles. **D.** Evaluation of the image using the "Scatter Plot" option. **E.** The diameter of the infection site is measured. **F.** The infection site was visualized from a majority of particles that is surrounding the cornea to make a circle and using the "Analyze" tool the diameter was measured.

Statistics

Scatterplot analysis data was analyzed using the Graph Pad InStat (GraphPad Software, San Diego, CA). Scatterplot diameters of the images were assessed using ANOVA, standard parametric analysis

of variance. Tukey's test was utilized to compare all pairs of columns. All experiments were with multiple eye samples. $P < 0.05$ was considered significant. Data were expressed as means ± the standard errors of the means (SEM).

Results and Discussion

Keratitis in mouse eyes is evident due to the opacity that is demonstrated in the cornea of the eye. The focus of the study was to determine if an assessment tool could be used to understand the spread of bacteria in a keratitis model. The study evaluates the use of ImageJ and its ability to analyze ocular images from mice infected with pneumococcal keratitis. ImageJ's image processing application was used to map the progression of keratitis infection in the aging mouse model from day 1 to day 5 post-infection. The analysis elucidated the damage associated with pneumococcal keratitis. The images in the study are from the experiments that followed the established scratch model mouse model.[12]

The ImageJ analysis was used to create a binary image, which demonstrates the area that is affected by the presence of the bacteria (opaque) versus health tissue (translucent). The outline of the keratitis infection illustrates the damage that occurs in the cornea (Figure 2). An eye trend map of infection was established with mice ocular images representing a variety of mice eyes of keratitis ranging from day 1 to day 5 post-infection (Figure 3). This tool can now be used in the future studies that want to analyze and compare infection progression in young and old mice.

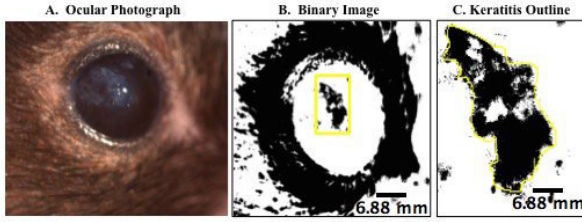

Figure 2 Analytical Exposure of Keratitis Image. **A.** Keratitis Image of infected mouse eye. **B.** Infected eye converted to binary image to reveal infection site. **C.** Enlarged view of Outline of Keratitis infection as seen in 1B.

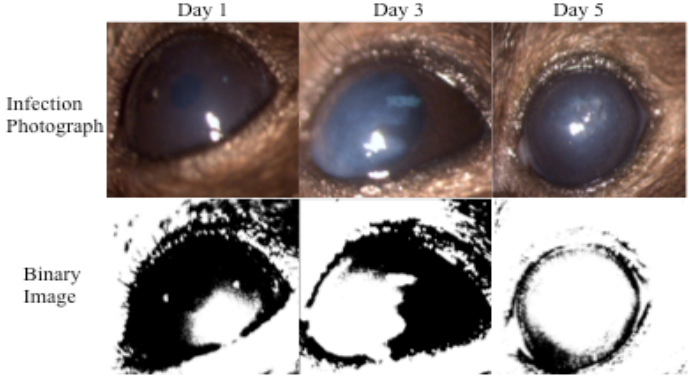

Figure 3 Binary Image analysis of 7-8 week C57BL/6 mice eyes on Days 1,3,and 5 post-infection. Binary image analysis comparison of keratitis infected mice eyes on day 1, day 3 and day 5-post-infection.

To further evaluate the impact of keratitis on the cornea of the mouse and to provide an alternate approach to studying keratitis, a scatter plot was performed (Figure 4). The scatterplot allowed for the spread of the infection to be measured. The data collected from the measurements was complied into a bar graph based on days post-infection starting at Day 1 and extending to Day 5; the results

indicate a significant increase occurs in the spread of the keratitis infection between Day 1 and Day 3 (Figure 5). Thus, the major impact of the keratitis infection occurs within the first 48 hours following infection. This data supports the need for early intervention to prevent irreversible damage.

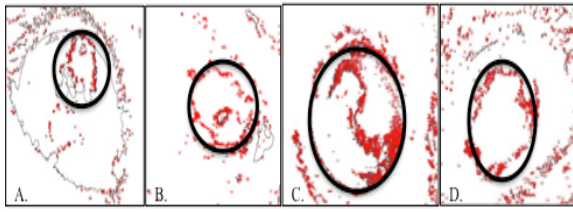

Figure 4 Scatter Plot Analysis of young and old eyes. **A.** Representative mild infection analysis for a young mouse cornea. **B.** Representative mild infection analysis of an old mouse cornea. **C.** Representative severe infection analysis of young mouse cornea. **D.** Representative severe infection analysis of old mouse cornea. The circle represents bacterial and bacterial products related damage of the cornea. The diameter of the scatterplot analysis was utilized for analysis.

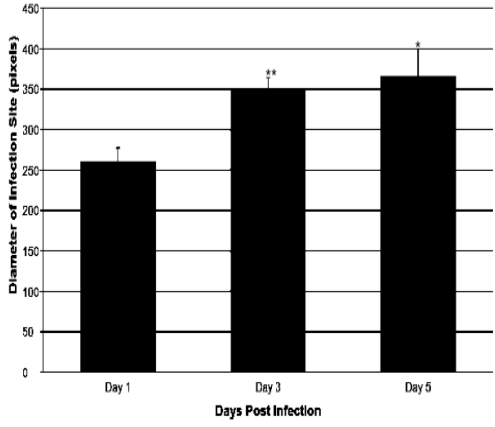

Figure 5 Diameter measurements of Scatter Plot analysis of infected corneas. The diameter scale demonstrated the spread of keratitis for day 1 vs. day 3; $p<0.05$, day 1 vs. day 5; $p<0.05$, day 3 vs. day 5; $p>0.05$.

This study has optimized and validated a standard protocol for analyzing keratitis in the murine model using the ImageJ Software. The S. pneumoniae bacteria progression towards the cornea as the days of the infection continued is now thoroughly documented and can be used as a baseline for future work. The study sets an alternative for studying the spread of infection for surface related infection models that could possibly reduce the number of animals utilized in an infection study. A disease computer model has been created to determine the results from the sequence of the events occurring post-infection. And timeline analysis has underscored the importance of early intervention in bacterial keratitis.

Acknowledgements

Department of Biology internal funding supported the work and the work is a part of the Cardiovascular and Microbiology Research Center.

References

1 Liesgang, T. in *The Cornea* (ed HE Kaufman) 217-270 (Churchill Livingstone, 1988).

2 Callegan, M. C., O'Callaghan, R. J. & Hill, J. M. Pharmacokinetic considerations in the treatment of bacterial keratitis. *Clin Pharmacokinet* **27**, 129-149, doi:10.2165/00003088-199427020-00005 (1994).

3 McLeod, S. D. *et al*. The role of smears, cultures, and antibiotic sensitivity testing in the management of suspected infectious keratitis. *Ophthalmology* **103**, 23-28 (1996).

4 Robinson, K. A. *et al*. Epidemiology of invasive Streptococcus pneumoniae infections in the United States, 1995-1998: Opportunities for prevention in the conjugate vaccine era. *JAMA* **285**, 1729-1735 (2001).

5 Ormerod, L. D. Causes and management of bacterial keratitis in the elderly. *Can J Ophthalmol* **24**, 112-116 (1989).

6 Ehrlich, R. *et al*. Age-related ocular vascular changes. *Graefes Arch Clin Exp Ophthalmol* **247**, 583-591, doi:10.1007/s00417-008-1018-x (2009).

7 Girgis, D. O., Sloop, G. D., Reed, J. M. & O'Callaghan, R. J. Susceptibility of aged mice to Staphylococcus aureus keratitis. *Curr Eye Res* **29**, 269-275, doi:10.1080/02713680490516783 (2004).

8 Hazlett, L. D., Kreindler, F. B., Berk, R. S. & Barrett, R. Aging alters the phagocytic capability of inflammatory cells induced into cornea. *Curr Eye Res* **9**, 129-138 (1990).

9 Rasband, W. S. *ImageJ*, <http://rsb.info.nih.gov/ij/> (1997).

10 Schneider, C. A., Rasband, W. S. & Eliceiri, K. W. NIH Image to ImageJ: 25 years of image analysis. *Nat Methods* **9**, 671-675 (2012).

11 Collins, T. J. ImageJ for microscopy. *Biotechniques* **43**, 25-30 (2007).

12 Moore, Q. C., 3rd *et al*. Development of a Streptococcus pneumoniae keratitis model in mice. *Ophthalmic Res* **42**, 141-146, doi:10.1159/000229028 (2009).

Proposing Drug Target(s) to Combat Trypanosoma brucei Infection

Taylor McGowen and Max Fontus

Prairie View A&M University

Corresponding Author: *Max Fontus, Texas Undergraduate Medical Academy, Prairie View A&M University, P.O. Box 519 MS 2900, Prairie View, TX, 77446; Phone: 936-261-3091; Email: mafontus@pvamu.edu*

Abstract

Background: Sub-Saharan African countries are plagued by an adaptable parasite, *Trypanosoma brucei, T.b.*, with a very high iron dependency. This protozoan parasite is the causative agent for Human African Trypanosomiasis (HAT), otherwise known as sleeping sickness. Two specific subspecies of interest include *T.b. gambiense* and *T. b. rhodesiense*. They lead to either a chronic or acute form of the fatal sleeping sickness disease, respectively. Few effective methods of treatment are available. The goal of this research project is to propose pharmaceutical drug target(s) to combat T. *brucei* infections. **Methods:** Studies analyzed the reaction pathways that take place during the parasite's life cycle, identified the natural and chemically produced superoxide radicals within the parasite, and also elucidated the differences in the parasite's life processes will allow for the derivation of a plausible methods to cease the infection cycle of the *T. brucei* parasite. The impact of these factors on preventing or reducing the virulence of the infection by T. *brucei* was assessed using computer-aided simulation software named *CLEMS*, Command-Line Electro-Metabolomics Software. We monitored the concentrations of oxygen, glucose and dihydroxyacetone phosphate, DHAP, given their importance for the survival of the parasite. Oxygen concentration peaked soon after the start of the simulation before achieving steady state with a concentration comparable to that of the mammalian environment simulated; glucose concentration was constant throughout the simulation again consistent with the environment where the parasite is evolving; finally, results showed a decrease in DHAP

concentration followed by steady state. Any process, which contributes to further decreasing DHAP concentration, is likely to be detrimental to the T. brucei. Other processes, such as superoxide radical degradation, will be considered in concert to the ones assessed in this study to develop suitable drug targets.

Introduction

Native to Sub Saharan African countries, the tsetse fly carries and transmits a fatal and often neglected tropical disease, Human African Trypanosomiasis, or HAT. This deadly disease affects at least 30 African countries.[1] The country with the highest infection rate is the Democratic Republic of Congo.[2] Of note, the number of reported cases of *Trypanosoma brucei gambiense* infections, which are chronic, is extremely higher than those of *T. b. rhodesiense*, which are acute. However, neither of these subspecies morphologically differs from one another.

The transmission route and life cycles are also important. A tsetse fly will ingest the parasite where it is transported to the gut. The parasite is then in the procyclic form while inside the fly. Once the fly is infected, the insect becomes a vector of transmission for the disease until the end of its life. When the infected fly bites a human, it transfers the parasite directly into the human's bloodstream. Once in the bloodstream, the *T. brucei* parasite converts to the bloodstream form and circulates throughout the host's blood vessels and tissues.[3] In this form, the parasite spreads to important mammalian fluids including: lymph and cerebrospinal fluid, along with those found in the placenta.[2] Symptoms include, but not limited to, fever, severe headaches, irritability, extreme fatigue, swollen lymph nodes and aching muscles and joints. The disease is diagnosed by finding the parasite in body fluid or tissue by microscopy.[4]

Current treatment options have certain limitations or harmful effects associated with each option. Certain drugs do not combat both the haemo-lymphatic and the meningo-encephalic stages of the sleeping sickness, all the while *T. brucei* has already begun to grow resistant to some treatments. Therefore, the need for a drug target that can

inhibit parasitic functions, preferably through distinct and parasite-specific reaction pathways inhibition, has increased in recent years.

Moreover, *T. brucei* possesses several unique characteristics that increase its survival rates. Naturally, every organism is comprised of multiple defense mechanisms. *T. brucei* is equipped with four superoxide dismutases—all requiring an iron, Fe, metal cofactor. Superoxide dismutases, SODs, are antioxidants used in the parasite's defense mechanism to rid itself of radicals via dismutation of superoxide radicals into hydrogen peroxide and molecular oxygen.[5] This particular mechanism has been the target of many drug treatments (table 1).

Table 1 Existing Treatment Options for HAT: Available drug treatments for HAT along with possible side effects. Known structures are depicted as to facilitate future docking studies.

Drugs	Stage of Disease	Strain	Additional Info	Structure
NECT nifurtimox-eflornithine combination therapy	Central Nervous System Stage	Gambiense	Nifurtimox used in treat of Chagas disease	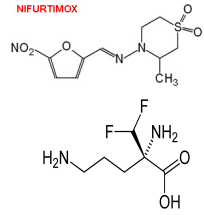
Pentamidine	Circulatory Stage	Gambiense	Side effect: effects on the pancreas	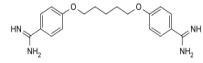
Eflornithine	Central Nervous System Stage	Gambiense	Side effect: Hematologic abnormalities,hearing loss, Thrombocytopenia	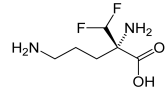
Melarsoprol	Central Nervous System Stage	Rhodesiense	Arsenic derivative Side effect: Convulsions, fever, loss of consciousness, rashes, bloody stools, nausea, and vomiting. Encephalopathy	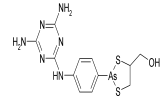
Suramin	Circulatory Stage	Gambiense and Rhodesiense	Side effects: rashes,adrenal cortical damage, kidney damage	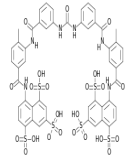

T. brucei, receives all of its energy from glycolysis. This glycolysis cycle differs from other eukaryotes in that glycolysis is *T. brucei*'s sole ATP-producing process.[6] The parasite metabolizes the glucose readily available in the host's bloodstream converting it into pyruvate. The first seven steps occur in the glycosome, a part of the cell with functions similar to peroxisomes.[6] Other eukaryotes carry out the process in the cell's cytosol. This peculiarity makes *T. brucei*'s glycolysis mechanisms one of the main foci for drug target analysis.[6,7] In addition, the parasite's glycolytic process can occur under both aerobic and anaerobic conditions. Some factors facilitating the parasite's adaptability include, yet not limited to: changes in coat surface and antigenic variation. The parasite exhibits antigenic variation, which is a switch in expression of variable surface glycoproteins, VSG, genes that encodes VSG coats.[3] These thick coats protect the parasite from immune system attacks. T. *brucei* has multiple VSG genes, only expressing them one at a time.[3] This particular adaptability contributes to the parasite's ability to bypass immunological responses and allows it to multiply in the mammalian bloodstream and eventually cross the blood-brain barrier. Unfortunately, minimal information is available on exact pathways during this switching process, and therefore much research is still needed. Current literature reveals that there are five existing treatment options for HAT (Table 1), and of the five some are either toxic to the host, too expensive for administration, or fails to address the infection in its entirety.

Chemotherapeutic drugs treat the disease by inducing oxidative stress (Table 1). A component of the most readily accepted treatment option, NECT, Nifurtimox leads to the formation of reactive oxygen species otherwise referred to as ROS.[8] The drug can be orally administered and is readily absorbed throughout the body crossing the blood-brain barrier.[9] Eflornithine, the other component of NECT combats the meningo-encephalic stage in *T. b. gambiense* infection but is ineffective against *T. b. rhodesiense*. The demand for a new pharmaceutical drug to combat sleeping sickness increases each day as the parasitic infection persists. To contribute to this search and study, computational modeling methods were used to assess impacts of reaction pathway disruptions. We simulated the glycolytic and the

superoxide radical degradation pathways of the parasite within the mammalian oxic environment.[7,10] We monitored the concentrations of oxygen, glucose and DHAP as these represent three of the most important compounds that T. brucei relies on for survival.

Materials and Methods

Mathematically derived models of reaction pathways were developed and utilized for computer simulation. Reaction kinetics data was obtained through extensive literature review. The parasites' dire need for iron and the occurrence of free radicals due to the superoxide radical degradation pathway are pertinent to the discovery of the pharmaceutical drug target to annihilate the parasite without harming the hosts. The superoxide radical degradation pathway acts like the electron transport chain, severing oxygen molecules resulting in extremely reactive oxygen radicals. Manipulating a reaction's pathway to produce reactive oxygen radicals would in turn cause the parasite to self-destruct. Chokepoints, which are metabolites at the end of a metabolic process used as in other reactions pathways, constitute a major aspect in developing an improved drug target. Thus, they were followed closely throughout the simulation. Enzymatic activities of the multiple biochemical and electrophysiological species of the parasite were accounted for with specific Michaelis-Menten parameters. The formula:

$$h = \frac{VKY}{AK(K + c + c') + (A\theta cc')}$$

provides a four-state model for a facilitated diffusion carrier. In the above equation, h is the parameter that quantifies how fast the species can navigate the membrane, V is the maximum rate of exchange of species between compartments, K is the Michaelis-Menten constant describing transport properties between compartments, c and c' are respective concentrations, and θ is the symmetry index between compartments. The value for θ can vary between the integers 0 and 1.[1]

Reactions that occur in the same cellular region or share some common species were classified, organized, and their kinetic values were computed. In addition, reactions were designated as either slow or fast, i.e. equilibrated. In the glycolysis pathway, 41 slow reactions that are taking places in three separate cell compartments were recorded and analyzed. The ATP-producing process that converts 2 moles of glucose into 2 moles of pyruvate is extremely intricate. Without the proper transportation of every compound and element, *T. brucei* suffers. Hence, proper identification of the location of each step in the process proves pertinent to calculations. The transportation of charged and rather large metabolites across an impermeable membrane dictates the usage of transporters. The transport of species against their gradients indicates active diffusion, which was modeled also in the simulation. The reactions were written in accordance to the mechanisms of the pathway. Parameters, such as maximum transport rate of a species from compartment to compartment, Michaelis-Menten constants, stoichiometry of reactions, and other specifications were calculated and calibrated, where information was incomplete, to give final concentrations of each species. Once all of the data was obtained and computed, the information was input into the *CLEMS* software (Max Fontus, Cypress, TX), where numerical datasets describing species concentrations at multiple time steps were produced. *CLEMS* generates quantitative data by converting biochemical and electrophysiological information into ordinary differential equations, which are then solved numerically.

All initial information was compiled[1,7] in a master list containing species name, molecular weight, formal charge, and chemical symbol; each species was assigned a numerical value within the simulation (Table 2). Throughout the simulations, different environments and conditions can be easily assessed and according results investigated.

Table 2 Species Master List: These are the species involved in the five known important pathways of T. *brucei*. The associated charged of the species are also tabulated when reported in the literature or based on the pH level of the compartment where they are located in the course of a simulation. The charges in the parentheses are reflective of the fact that multiplicity of charges is possible based on pH

Species Name	Species number	Chemical Symbol/ formula	Charge	MW (g/mol)
Dihydroxyacetone phosphate (DHAP)	1	$C_3H_7O_6P$	0(-2)	170.06
Glucose	2	$C_6H_{12}O_6$	0	180.16
Glucose 6 phosphate (Glc-6-P)	3	$C_6H_{13}O_9P$	0(-2)	260.16
Fructose 6 phosphate (Fru-6-P)	4	$C_6H_{13}O_9P$	0(-2)	259.81
Fructose 1,6-bisphosphate (Fru-1,6-BP)	5	$C_6H_{14}O_{12}P_2$	0(-4)	340.116
Glyceraldehyde 3-phosphate (GA-3-P)	6	$C_3H_7O_6P$	0(-2)	170.058
1,3-bisphosphoglycerate (1,3-BPGA)	7	$C_3H_8O_{10}P_2$	0(-4)	266.03
3-Phosphoglycerate (3-PGA)	8	$C_3H_7O_7P$	0(-2)	186.06
2-Phosphoglycerate (2-PGA)	9	$C_3H_7O_7P$	0(-2)	186.06
Glycerol 3-Phosphate (Gly-3-P)	10	$C_3H_9O_6P$	0(-2)	172.074
Phosphoenolpyruvate (PEP)	11	$C_3H_4O_6P$	-1(-3)	167.034
Fructose 2,6-bisphosphate (F26BP)	12	$C_6H_{14}O_{12}P_2$	0(-4)	340.116
Hexokinase (HK)	13	Enzyme		
Phosphoglucose Isomerase (PGI)	14	Enzyme		
Phosphofructokinase (PFK)	15	Enzyme		
Aldolase (Ald)	16	Enzyme		
Triose Phosphate Isomerase (TIM)	17	Enzyme		
Phosphoglycerate Kinase (PGK)	18	Enzyme		

Table 2 Continued

Species Name	Species number	Chemical Symbol/ formula	Charge	MW (g/mol)
Glycerol 3-Phosphate Dehydrogenase (G3PDH)	19	Enzyme		
Glycerol Kinase (GK)	20	Enzyme		
Adenylate Kinase (AK)	21	Enzyme		
AMP-activated Protein Kinase (AMPK)	22	Enzyme		
Glyceraldehyde 3-Phosphate Dehydrogenase (GAPDH)	23	Enzyme		
Pyruvate Kinase	24	Enzyme		
Glycerol 3-Phosphate Oxidase (GPO)	25	Enzyme		
Enolase (ENO)	26	Enzyme		
Adenosine Triphosphate (ATP)	27	$C_{10}H_{16}N_5O_{13}P_3$	-4(-3)	507.18
Adenosine Diphosphate (ADP)	28	$C_{10}H_{15}N_5O_{10}P_2$	-3	427.201
Adenosine Monophosphate (AMP)	29	$C_{10}H_{14}N_5O_7P$	-2	347.22
Cyclic Adenosine Monophosphate (cAMP)	30	$C_{10}H_{12}N_5O_6P$	-1	329.206
Hydrogen Gas, H_2	31	H_2	0	2.016
Proton, H^+	32	H^+	+1	1.008
Sodium ion, Na^+	33	Na^+	+1	22.990
Potassium ion, K^+	34	K^+	+1	39.098
Chlorine ion, Cl^-	35	Cl^-	-1	35.453
Oxygen gas, O_2	36	O_2	0	31.998
Water, H_2O	37	H_2O	0	18.015
Nicotinamide Adenine Dinucleotide, NAD+	38	$C_{21}H_{27}N_7O_{14}P_2$	-1	663.43
Reduced Nicotinamide Adenine Dinucleotide, NADH	39	$C_{21}H_{28}N_7O_{14}P_2$	-2	664.44
Pyruvate (Pyr)	40	$C_3H_4O_3$	-1	88.06
Glycerol (Gly)	41	$C_3H_8O_3$	0	92.09
Inorganic Phosphate, P_i	42	PO_4	-1	82.16
Phosphoglycerate Mutase (PGM)	43	Enzyme		
Ald-FBP	44			

Table 2 Continued

Species Name	Species number	Chemical Symbol/ formula	Charge	MW (g/mol)
Ald-DHAP	45			
END	46			
G3PDH-NAD	47			
EGN	48			
ESTE	49			
PAP	50			
ATP-PyK	51			
GAG	52			
ATP-GK	53			
PHD	54			
PHA	55			
PAMBG	56			
ATP-PGK	57			
PAMF	58			
ADP-PFK	59			
ESTPi	60			
HGAM	61			
ADP-HK	62			
ATP-HK	63			
ATP-PFK	64			
G3PDH-NADH	65			
ADP-GK	66			
PFKna	67			
ADP-PGK	68			
ADP-PyK	69			
GAPDH-GAP	70			
PHA*	71			
Nicotinamide adenine dinucleotide phosphate (NADP+)	72	$C_{21}H_{29}N_7O_{17}P_3$	-3	744.413
Reduced Nicotinamide adenine dinucleotide phosphate (NADPH)	73	$C_{21}H_{29}N_7O_{17}P_3$	-4	
6-Phosphogluconolactone (6-PGL)	74		0	
6-Phosphogluconate (6-PG)	75		0	
Ribulose 5-phosphate (Rul-5-P)	76	$C_5H_{11}O_8P$	+1	230.11
Ribose 5-phosphate	77	$C_5H_{11}O_8P$	+1	230.11
Carbon dioxide (CO_2)	78	CO_2	0	44.01

Table 2 Continued

Species Name	Species number	Chemical Symbol/ formula	Charge	MW (g/mol)
Trypanothione disulfide (TS_2)	79	$C_{27}H_{47}N_9O_{10}S_2$	0	721.84
Trypanothione [$T(SH)_2$]	80	$C_{27}H_{49}N_9O_{10}S_2$	-1	723.86
Ribose (Rib)	81	$C_5H_{10}O_5$	+2	150.13
Superoxide	82	O_2^{-1}	-1	32
Hydron,H^+	83	H^+	+1	1.008
Hydrogen peroxide	84	H_2O_2	0	3.015
Oxygen	85	O_2	0	16
Iron Superoxide Dismutase	86	Enzyme		
Superoxide Dismutase	87	Enzyme		

Results

Many species' concentrations oscillate until equilibrium is achieved. It can be observed that in glycolysis, the concentration of oxygen increases until it peaks, then decreases until steady state is achieved (figure 1). Oxygen is available in all compartments of the cell at all times, which would explain the major rise in the concentration until equilibrium is reached. Glucose concentration was constant, which is consistent with the fact that the mammalian host environment has a steady glucose concentration so that the parasite has a continuous source of metabolic fuel.

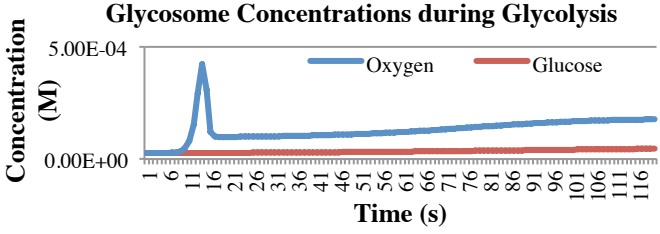

Figure 1 Concentrations of Oxygen and Glucose in the glycosome during a simulated glycolysis taking place in the mammalian bloodstream. These numbers were comparable to that of Navid[1,7]

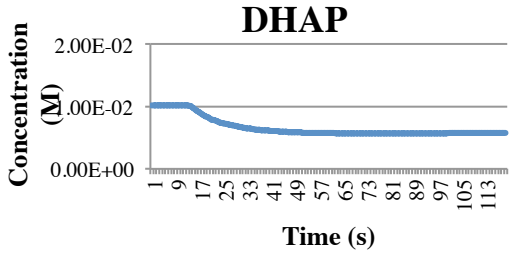

Figure 2 Concentration of DHAP in the glycosome during glycolysis where the conditions are the same as figure 1

The behavior of DHAP was monitored, given its importance in the anoxic, as well as anoxic, developmental conditions for the parasite. The obtained behavior of DHAP differed slightly from other factors. It started out almost constant; it then decreased until the concentration reached equilibrium between 5.00e-3 and 6.00e-3 M (figure 2). Any process contributing to further decrease in the concentration of DHAP would likely prove to be detrimental to the parasite.

Separate trials were run to validate the software by comparing its results to experimental historical data. Glycolysis was simulated by itself, but later on simulations involving glycolysis and the superoxide degradation pathway were done (Results not shown). This was designed to address the intertwining network of pathways *T. brucei* utilized to survive in multiple environments.

Conclusions

Glycolysis and superoxide radical degradation pathways were simulated in a computational environment based upon data from published literature. Given the importance of glycolysis, the parasite's sole ATP production process, and the superoxide radical degradation pathway, a chokepoint related to both pathways is believed to present and would be an ideal options for pharmaceutical drug target(s). This putative data confirms that inhibition of

glycolysis would lead to the destruction of *T. brucei*. Examination of additional chokepoints specific to each pathway is underway.

SODs are a major component of the defense mechanism in *T. brucei*. Analysis of the biochemical and molecular properties of mechanisms similar to the superoxide degradation pathway within the parasite is expected to provide better insights and holds promise for improved treatment intervention.

Unfortunately, HAT is a neglected disease in that it is not studied as much and subsequent studies tend to be unorganized. Specifics about the parasite in both life stages are not readily available and thusly cannot be used as part of the master input file, leading to an obvious limitation. However, having a fully functional and consistent electrophysiological model for *T. brucei*'s pathways and metabolism is of great significance. The parasite's high adaptability provides many such pathways and characterizes its greatest defense mechanism. Therefore, modeling other pertinent pathways taking place in *T. brucei* will expand and improve results from this project. With this tool, proposed mechanism(s) can be simulated for relevance. Once a mechanism is assessed, a target can be hypothesized. Drugs can be developed and simulated so that their capacity to eliminate or reduce infectivity, without negatively affecting the human host, can be studied well in advance of animal or human clinical trials.

Acknowledgements

This work was supported by Dr. Felecia Nave and Audie Thompson's REU program at Prairie View A&M University. The authors would also like to thank Dr. Max Fontus for his direction and Texas Undergraduate Medical Academy for the laboratory space and resources.

References

1 Navid, A. & Ortoleva, P. J. Simulated complex dynamics of glycolysis in the protozoan parasite Trypanosoma brucei. *J Theor Biol* **228**, 449-458, doi:10.1016/j.jtbi.2004.02.007 (2004).

2 Franco, J. R., Simarro, P. P., Diarra, A. & Jannin, J. G. Epidemiology of human African trypanosomiasis. *Clin Epidemiol* **6**, 257-275, doi:10.2147/CLEP.S39728 (2014).

3 Munday, J. C., Settimo, L. & de Koning, H. P. Transport proteins determine drug sensitivity and resistance in a protozoan parasite, Trypanosoma brucei. *Front Pharmacol* **6**, 32, doi:10.3389/fphar.2015.00032 (2015).

4 Buscher, P. *et al*. Sensitivity and specificity of HAT Sero-K-SeT, a rapid diagnostic test for serodiagnosis of sleeping sickness caused by Trypanosoma brucei gambiense: a case-control study. *Lancet Glob Health* **2**, e359-363, doi:10.1016/S2214-109X(14)70203-7 (2014).

5 Dufernez, F. *et al*. The presence of four iron-containing superoxide dismutase isozymes in trypanosomatidae: characterization, subcellular localization, and phylogenetic origin in Trypanosoma brucei. *Free Radic Biol Med* **40**, 210-225, doi:10.1016/j.freeradbiomed.2005.06.021 (2006).

6 Bakker, B. M., Westerhoff, H. V., Opperdoes, F. R. & Michels, P. A. Metabolic control analysis of glycolysis in trypanosomes as an approach to improve selectivity and effectiveness of drugs. *Mol Biochem Parasitol* **106**, 1-10 (2000).

7 Bakker, B. M., Michels, P. A., Opperdoes, F. R. & Westerhoff, H. V. Glycolysis in bloodstream form Trypanosoma brucei can be understood in terms of the kinetics of the glycolytic enzymes. *J Biol Chem* **272**, 3207-3215 (1997).

8 Wilkinson, S. R. *et al*. Functional characterisation of the iron superoxide dismutase gene repertoire in Trypanosoma brucei. *Free Radic Biol Med* **40**, 198-209, doi:10.1016/j.freeradbiomed.2005.06.022 (2006).

9 Prathalingham, S. R., Wilkinson, S. R., Horn, D. & Kelly, J. M. Deletion of the Trypanosoma brucei superoxide dismutase gene sodb1 increases sensitivity to nifurtimox and benznidazole.

Antimicrob Agents Chemother **51**, 755-758, doi:10.1128/AAC.01360-06 (2007).

10 Fang, J. & Beattie, D. S. Alternative oxidase present in procyclic Trypanosoma brucei may act to lower the mitochondrial production of superoxide. *Arch Biochem Biophys* **414**, 294-302 (2003).

Agricultural Vinegar as a growth control agent for both Glyphosate susceptible (GS) *Amaranthus palmeri* and Glyphosate resistant (GR) *Amaranthus palmeri*

Frank Garcia and Yolander Youngblood, Ph.D.

Prairie View A & M University

Corresponding Author: Yolander Youngblood, Ph.D., Department of Biology, Prairie View A & M University P.O. Box 519, MS 2210, Prairie View A&M University, Prairie View, TX 77446; Phone: 936-261-3169; Email: yryoungblood@pvamu.edu

Abstract

Background: Annually farmers in the United States suffer crop losses due to the invasive weed, *Amaranthus palmeri*. The two major reasons for the losses are: the rapid reproduction and adaptability of this aggressive species. The dioecious *Amaranthus* has adapted so rapidly that some populations of *Amaranthus* are resistant to the traditional glyphosate herbicides. Glyphosate was introduced as an herbicide and was considered unlikely to cause resistant populations of plant species. The mechanism of action, lack of metabolic degradation in plants or residual activity in the soil made it a very popular herbicide hoice. Over time glyphosate resistant (GR) *Amaranthus palmeri* species emerged. This new GR *Amaranthus palmeri* calls for a new herbicide, preferably an organic herbicide. Agricultural Vinegar (vinegar with 20% acetic acid) is an effective, non-selective organic herbicide. Over time, a buildup of acetic acid may cause harm to the ecosystem. **Methods:** We are looking at organic herbicide solutions that contain lesser concentrations of acetic acid. For this experiment, we used solutions with 5%, 10%, and 20% acetic acid. These solutions were applied when the plants were young (less than 10 days) and less than 4 cm tall. We are observing the effects of the solution on the epicuticular wax and epidermal layers. We hypothesized that when applied very early, lower concentrations of agricultural vinegar (5%, 10%, or

15%) can slow or stop growth and allow for the desired crop to outcompete the weeds.

Introduction

Amaranthus is a fast-growing C4 (stores carbon as malate) annual weed that can grow up to 10 feet in height.[1] Due to the over-reliance of the chemical glyphosate (Round up™) to combat weeds, many strains of *Amaranthus* have shown signs of glyphosate resistance. Of the glyphosate resistant (GR) plants discovered, *Amaranthus palmeri* commonly known as "Palmer Amaranth" or "careless weed", is the most economically damaging to farmers because of its abilities to produce copious amounts of seeds, adapt quickly, and exhibit allelopathic tendencies towards crops. Further the leaves of *Amaranthus* plants can use diaheliotropism to maximize its photosynthetic capacity and result in extreme heights.[2] Palmer amaranth also exerts allelopathic effects to cause an inhibition of growth in carrots, onions, cabbage, and other plants.[2] These attributes allow the plant to grow quickly and cause billions of dollars to be wasted in yield losses.[3]

This plant possesses the ability to stave off incomplete physical control measures while still growing to produce viable seeds. Prior studies show that *Amaranthus* plants could regenerate after suffering the trauma of physical control measures.[4] Examples of physical control measures are hand weeding and tilling. Tilling the fields affects not only the emerging weeds but also the germination of the dormant seeds and the weed seed bank in the soil.[5] In one experiment, a control plant along with individuals that had their stems cut to heights of 15 cm, 3 cm, and 0 cm above the soil to see their regenerative properties was utilized. At the end of the experiment, the plant that was cut all the way to the soil was still able to produce 23,000 seeds despite a 95% mortality rate, whereby just 5% survived.[4] There is much concern over the ability of many *Amaranthus* plants to bounce back from physical or chemical control measures. One plant can produce anywhere from 200,000-300,000 seeds.[4] If 95% of the seeds die during the winter months, then 5% of the plant remains. If the farmer then kills 99% of the remaining

weeds, the farmer will still have more than 3000 pig weed plants to deal with in the future.[6]

Rise of the Resistance

Glyphosate was considered an ideal herbicide for *Amaranthus* plants, because its chemical properties minimized resistance and its mechanism of action meant an absence of metabolic degradation in plants and a lack of residual activity in the soil.[7] *A. palmeri* is a dioecious plant, meaning each individual contains one or the other reproductive organs requiring two separate plants to reproduce.[1] This allows the plant to have the innate ability to increase its genetic diversity giving it an evolutionary advantage in overcoming the stresses of herbicides.[8]

Over time the first GR *Amaranthus* plants emerged in the state of Georgia in 2005.[7] Not all species of *Amaranthus palmeri* were glyphosate resistant. Others were still susceptible to glyphosate herbicides (GS *Amaranthus palmeri*). In the seven subsequent years, GR *Amaranthus palmeri* spread from North Carolina to California. Research showed that *Amaranthus* had built up a resistance to not only glyphosate but also ALS (acetolactate synthase) herbicides, EPSPS (5-enolpyruval-shikmate synthase) herbicides, and other herbicides that operate by affecting the photosystem II in plants.[4] While a strain of *Amaranthus* that is resistant to ALL herbicides has not be found, the fact is it is possible that plants can become resistant after repeated use.[1] Plants can become resistant to glyphosate through target site and non-target site mechanisms.[2] Target site resistance is attributed to altered glyphosate herbicide interaction with the target enzyme. Non-target site resistance is due to altered translocation within the plant, and altered translocation is reported to be the most common mechanism of resistance.[4,7] Herbicides select for resistance in the populations by killing off all other genetic competition; farmers unwittingly create an artificial selective pressure increasing the odds that Palmer amaranth will become resistant.[9]

The invention and propagation of Round up™ (glyphosate)-ready technology allowed the overuse of glyphosate herbicides. The

technology also initially increased production in the agricultural sector, as it was used in 85% or more of the soybeans and 95% or more of the cotton crops.[9] However, this means these same fields are now prone to resistant weeds, the rising of which could dramatically affect production and cost to the public.

Organic Growth Control Agents

Recently there has been increased consumer interest in organic vegetables. In meeting this demand, many organic herbicides have been developed to assist the organic farmer in his ever-evolving struggle against undesirable weeds. These herbicides use many different pathways to kill their selected target. Corn gluten meal, for example, is a byproduct of corn processing whose composition of 60% protein and 10% nitrogen, coupled with its herbicidal properties, make this organic herbicide a good weed and feed.[10] Microbial herbicides like Phoma Macrostoma Stain, are weak plant pathogens. Macrostoma works by colonizing the leaves and secreting compounds called macrocidins that bleach the leaves, causing chlorosis. Streptomyces is another microbial utilized for weed management. This microbe is produced in a facility where the organism's secretions are harvested after it produces them. The secretions are then used for its herbicidal properties.[10] However, in recent years, fear over possible mutations has slowed the growth in microbial herbicides.

Agricultural vinegar is a relatively recent addition to the organic herbicide market. A popular brand Weed Pharm™ is 20% acetic acid. The acetic acid is applied to the weeds that are targeted for termination. The herbicide has shown great promise killing *Amaranthus retroflexus*.[10] In multiple studies, 20% agricultural vinegar concentrations were able to completely kill weeds after nine days of treatment.[10] When applied to the leaves, the acetic acid eats through the leaf surface, including the epicuticular wax and cuticle. The long-term effects of acetic acid deposition to the soil or to the other organisms in the environment are unknown. Considering this fact, the minimal concentration of acetic acid should be used when or if possible. The earlier a herbicide is applied, the more effective it will be. The *Amaranthus* plants are often already 12 inches high

before farmers start weeding, so another step would be to be able to intervene earlier in the growth cycle.[11]

Hypothesis –Agricultural vinegar concentrations of less than 20% acetic acid can serve as effective growth control agents for both GS *Amaranthus palmeri* and GR *Amaranthus palmeri*.

Materials and Methods

Varying concentrations of acetic acid (5%, 10%, and 20%) were used as a means of controlling the growth of both GS *A. palmeri* and GR *A. palmeri*. Since 20% seems to be an effective industry standard, that concentration was used as a standard of practice control, and two lower concentrations were compared. As this was a preliminary study, a non-treatment control group was not used (plants treated with only water).

All seeds were planted in 905 cm^3 pots with Miracle Gro© Potting Soil, that contains pre-mixed fertilizer.

A new batch of plants were seeded every week for seven weeks. Cycle 1 consisted of planting 10 pots of glyphosate susceptible (GS) *A. palmeri* and 10 pots of GR *A. palmeri*. Cycle 1 was watered 2 times per week.

Cycle 2 consisted of 10 pots of GS *A. palmeri* only, and another 10 pots with GS *A. palmeri* coupled with beans. Beans were seeded to see how they would respond to the 5% acetic acid along with being placed with the GS plants. Cycles 3 and 4 each contained 10 pots of GR *A. palmeri* and 10 pots of the GS strains. Cycle 2 and all subsequent weeks were watered only once a week.

All the vinegar was prepared from mixing 100% acetic acid with deionized water except for the 5% table vinegar. To procure the 5% acetic acid, Heinz distilled white vinegar was purchased. For the stronger concentrations, 20 mL 100% acetic acid was mixed with 180 mL deionized water to achieve 200 mL of a 10% acetic acid

solution. To make the 20% acetic acid solution, 40 mL of 100% acetic acid was mixed with 160 mL deionized water.

The application of acetic acid took approximately ten (10) Days, where Day 0 was the day each cycle was planted. Cycles 1 and 2 received 5% acetic acid by volume, which was applied to leaves via a spray bottle. Cycle 3 received 10% acetic acid by volume applied directly to the leaves *and hypocotyl* of the plants. The application of acetic acid on the hypocotyl was do the lack of growth uptained in the greenhouse from the Amaranthus species. The majority of the plants did not develop true leaves, so the acetic acid was applied to the cotyledons and the hypocotyl. The 4th cycle received the 20% acetic acid solution applied in the same manner as the 10% solution.

Results and Discussion

The average height for each plant sprayed was about 4cm tall (Table 1). The research suggested that 20% concentration of acetic acid was already established as an excellent means of control for *Amaranthus* plants, so this investigation aimed to elucidate the lowest effective concentration. Through the course of the experiments, three different concentrations of acetic acid were applied to the susceptible and resistant *Amaranthus* plants: 5%, 10%, & 20%. The 20% and the 10% concentrations of acetic acid were most effective at killing the young amaranth, less than 21 days old. The 20% acetic acid solution took less than 24 hours to kill the entire sample on which it was sprayed. While the 10% acetic acid solution killed a majority of the plants on which it was sprayed, it was not 100% effective. In Cycle 3, the 10% solution reduced the total overall GS weed number by 85% and killed all GR plants. The 5% solution was not very effective. Plants who received 5%, did have a significant amount of mycelium growth in the pots. The specific effect of the mycelium growth is unknown.

Table 1 Amaranthus Growth Chart. Plants grown in June and July 2016

Day	Type	# of Plants	Height	# of Leaves
Day 3	Cycle 1 R	< 10	1 cm	2
Day 3	Cycle 1 S	> 30	1 cm	2
Day 7	Cycle 1 R	< 10	2.5 cm	2
Day 7	Cycle 1 S	< 15 in all but 2 water damage	3.5 cm	2
Day 9	Cycle 1 R	< 10	4 cm	2
Day 9	Cycle 1 S	< 10	3.5 cm	2
Day 9	Cycle 2 S	No New Growth	No Growth	0
Day 9	Cycle 2 S & Beans	No New Growth	No Growth	0
Day 15	Cycle 1 R	2 pots > 10 8 pots < 5	2.5 cm	2
Day 15	Cycle 1 S	< 10 in all pots water really hurt them	3.5 cm	2
Day 15	Cycle 2 S	5 pots > 20 1 pot 15 4 pots < 10	1/2 3.5 cm 1/2 4 cm	2
Day 15	Cycle 2 S & Beans	4 pots > 30 2 pots about 15 4 pots < 10	3.5 cm Avg. bean 23 cm	2
Day 16	Cycle 1 S	< 5 in all pots	3.5 cm	2
Day 16	Cycle 2 S	All sprayed 5% acetic acid (2 sprays)	4 cm	2
Day 28	Cycle 1 S	< 5	4 cm	2
Day 28	Cycle 2 S & Beans	< 20	4 cm	2
Day 28	Cycle 3 S	10 pots > 30	3.75 cm	2
Day 28	Cycle 3 R	5 pots about 15 & 5 pots about 10	3.5 cm	2
Day 29	Cycle 3 R&S	6 of Cycle 3 sprayed 10% acetic acid	3.5 cm	2
Day 31	Cycle 1 R&S	Same	4 cm	2
Day 31	Cycle 2 S	Same	4 cm	2
Day 31	Cycle 3 R	Same	4 cm	2
Day 31	Cycle 3 S	10 pots > 25	3.75 cm	2

Table 1 Continued

Day	Type	# of Plants	Height	# of Leaves
Day 35	Cycle 1 R&S	Same	4 cm	2
Day 35	Cycle 2 S	Same	4 cm	2
Day 35	Cycle 3 R	Same	4 cm	2
Day 35	Cycle 3 R sprayed	0 (Dead)	0 cm	2
Day 35	Cycle 3 S	Same	4 cm	
Day 35	Cycle 3 S sprayed	< 5	4 cm	2
Day 35	Cycle 4	> 30	4 cm	2
Day 35	Cycle 4	< 15	4 cm	2
Day 36	Cycle 4	Half of each sprayed w/20% acetic acid	4 cm	2
Day 37	Cycle 1 R & S	Same	4 cm	2
Day 37	Cycle 2 S & Beans	Same	4 cm	2
Day 37	Cycle 3 R & S	Same	4 cm	2
Day 37	Cycle 4 S not sprayed	> 20	4 cm	2
Day 37	Cycle 4 R & S sprayed	0 (Dead)	0 cm	2

R = Resistant S= Susceptible

The results indicate that 10% concentrations could be used, and further research could scale studies on concentrations of 18%, 16%, 14%, and 12% to further refine the impact of the solutions on weed growth.

The JCM 5000 NeoScope™ tabletop scanning electron microscope (SEM) was used to analyze images of each experimental group to document the physiological changes, if any, to the epicuticular waxes located on the leaves. Micrographs of the adaxial leaf surface were taken before and after the application of the varying concentrations of acetic acid to document the change in the sample. This gave a viable overall picture of the effectiveness of each varying concentration of acetic acid.

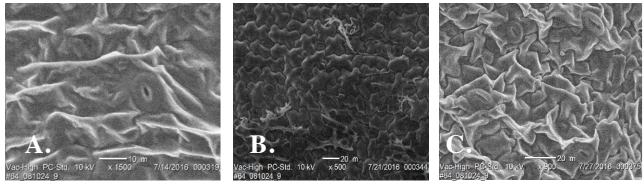

Figure 1. Scanning Electron Micrographs of *Amaranthus palmeri* leaves. **A.** 5% Acetic Acid Applied (Day 14). **B.** No vinegar (Day 14). **C.** 20% Acetic Acid (Day 10). Note changes in epidermal cells. Samples A) and C) are comparable in that there are changes. Sample B) represents the typical leaf surface with no damage.

The SEMs taken corresponded with the data collected (See the SEM's in Figures 1). All of the samples that were sprayed with acetic acid showed signs of stress regardless of the concentration. Figure 1A shows deformation in the dermal layer cells that occurred in the leaves when sprayed with 5% acetic acid. It took 14 days to show this change. While the 5% did cause some changes to the cuticle layer, the effects of the 20% acetic acid solution were seen earlier and were more significant (Figure 1C). The high dosage of acetic acid caused massive plasmolysis (loss of structure due to dehydration) in the upper layers of cells resulting in a loss in turgor pressure causing wilting as seen in Figure 1C; this process culminated in plant death. In Figure 1B you can see normal cells that look taut and rigid in comparison to its counterparts. This was to be expected in the sample with no exposure to acetic acid.

Conclusions

Overall, the experiments show that if caught early enough, with in the first 30 days, the young *A. palmeri* may be treated with applications of 10% acetic acid or 20% acetic acid regardless of its glyphosate resistance. This is beneficial for the environment because it will decrease the buildup of acetic acid in the soil. This minimizes the chance for making the soil and surrounding environment more acidic. It also brings down the price per acre of producing produce. This in turn brings down the price at the supermarket. Future work

can refine what concentration between 10 and 20% remains effective, and further analysis of how the herbicide affects the soil could also lead to more discovery, optimization and further savings.

Acknowledgements

The Summer Research Experience Program (SREP) at Prairie View A&M University supported this research. Special thanks are given to Dr. Thompson and the Department of Biology.

References

1 Morichehette, S., Ferrell, J. & Leon, R. *University of Florida: IFAS Extension*, <http://edis.ifas.ufl.edu/> (2012).
2 Chahal, P., Aulakh, J., Jufulam, M. & Jhala, A. in *Herbicides, Agronomic Crops and Weed Biology* (eds A Price, J Kelton, & L Sarunaite) (2015).
3 Jabran, K., Mahajan, G., Sardana, V. & Chauhan, B. Review: Allelopathy for weed control in agricultural systems. *Crop Protection* **72**, 57-65 (2015).
4 Sosnoskie, L., Culpepper, A., Grey, T. & Webster, T. Severed stems of Amaranthus palmeri are capable of regrowth and seed production in Gossypium hirsutum. *Annals of Applied Biology* **165**, 147-154 (2014).
5 Morrison, L. Herbicide-resistant weeds: the tillage dilemma. *Corn & Soybean Digest* **74**, 24-30 (2014).
6 Roberson, R. Pigweed control is a numbers game. *Southeast Farm Press* **39**, 1 (2012).
7 Whitaker, J., Burton, J., York, A., Jordan, D. & Chandi, A. Physiology of Glyphosate-Resistant and Glyphosate-Susceptible Palmer Amaranth (Amaranthus palmeri) Biotypes Collected from North Carolina. *International Journal of Agronomy*, 1-6 (2013).
8 Legleiter, T. & Johnson, B. (ed Purdue Extension) (https://www.extension.purdue.edu/extmedia/ws/ws-51-w.pdf, 2013).
9 Yancy, J. Weed scientists develop plan to combat glyphosate resistance. *Southeast Farm Press* **32**, 1 (2005).

10 Quarles, W. *The IPM Practitioner: Monitoring the Field of Pest Mangement*, <http://www.birc.org/MayJune2010.pdf> (2010).
11 Smith, R. Herbicide resistance changing Sunbelt production options. *Southeast Farm Press* **40**, 1 (2013).

ABOUT THE AUTHORS

Falonne Moumbogno T. **Colbie** graduated from Prairie View A&M University (PVAMU) in spring 2016. Her research interests include the metal-histidine interaction and its application.

Alexandra **Cromer** is a senior, chemistry major at PVAMU and is slated to graduate in May 2018. She is interested in biomedical research and medical school.

Miles **Dubose** participated in the 2016 Summer Research Experience Program for High School Students (REH).

Dr. Hua-Jun **Fan** has been an Associate Professor in the Department of Chemistry at PVAMU since 2004. His research interests include the application of nanocomposite materials in the sustainable energy and security.

Dr. Max **Fontus** is the senior Assistant Director of the Texas Undergraduate Medical Academy and faculty member in the Department of Chemistry at PVAMU. Dr. Fontus has conducted research in the areas of microbial fuel cell technology, Systems biology, electrophysiogical/metabolomic modeling, and algebraic number theory. Lately, his research interests has reached the public and urban health sectors as well as individualized K-12 education where Cultural Responsive Educational Theories are used as pedagogical tools to increase the participation of minority groups in science, technology, engineering, and mathematics (STEM).

Frank **Garcia** is a senior, biology major at PVAMU. He is interested in attending graduate school and studying Fungal Ecosystems. He is fascinated with ecology and how the big picture of life moves. He hopes to change his research from weeds to fungi in graduate school.

Dr. Cleveland O. **Lane**, Jr. is an Assistant Professor in the Department of Biology at PVAMU. His research interests are STEM teacher and professional development, biological education, virtual

reality learning environments, Inquiry learning environments in undergraduate education and spatial learning.

Taylor **McGowen** is a chemical engineering major at PVAMU. Taylor has conducted research at North Dakota State University and at PVAMU. She has been a regional officer for the National Society of Black Engineers (NSBE), vice-president of the Purple Jackets- a female civic leadership organization at PVAMU, a member of Tau Beta Pi, engineering honor society, the Honors programs at PVAMU, and a member of the Texas Undergraduate Medical Academy. Taylor has studied Mandarin for three years at PVAMU.

Dr. Quincy C. **Moore** III is an Associate Professor in Biology at PVAMU with research interests in host pathogen interactions, microbiome, computational biology and novel therapies of ocular infections.

Emmanuel B. **Olorunyomi** performed his research as an undergraduate biology major and also participated in the LSAMP program.

Nia **Parker** graduated from PVAMU in spring 2017 and is currently working at Los Alamos National Lab as a Summer Intern. She is interested in renewable energy and security.

Steven **Wang** is a high school student at Cypress Ranch High School. He joined Dr. Fan's group as an REH Summer Intern in the Department of Chemistry at PVAMU in 2016.

Dr. Hao **Wu** is a visiting scholar at PVAMU from the School of Chemical Engineering at the Ningbo University of Technology in China. His research interest is synthetic organic chemistry.

Dr. Yolander **Youngblood** is an Assistant Professor in biology at PVAMU with research interests that include studying plant structures of culturally important plants such as *Amaranthus palmeri* and the education of urban students.

ACKNOWLEDGMENTS

We extend special thanks to the publishing specialist, Rochelle L. Williams, Ph.D., and Copyright Editor, Michelle S. Gehring, Ph.D.

We also want to acknowledge our reviewers for this inaugural issue.

Reviewers

Greggory Bernard, Ph.D.
Bianca Garner, Ph.D.
Kamilah Grant, Ph.D.
Jacquelyn Jackson, Ph.D.
Lauren King, Ph.D.
Tonya McKinney, Ph.D.
Megumi Mills, Ph.D.
Tonye Numbere, Ph.D.
Edward Omolo, Ph.D.
Quincy Quick, Ph.D.
Melissa Sanders, M.D.
Derrick Scott, Ph.D.
Bidisha Sengupta, Ph.D.
Angee Monique Taylor, Pharm. D.
Justin Thornton, Ph.D.
Shari Walker, Ph.D.
C. Ellen Washington, Ph.D.
Andrea White, D.D.S.

EDITORIAL BOARD